Full Length Article

Study on the novel green magnetoplumbite-type oxide $BaZn_{6-x}Ni_xTi_6O_{19}$: synthesis, structure and properties

Zhiwei Wang [a], Liangsheng Tian [a], Suwit Suthirakun [b], Wongsathorn Kaewraung [b], Anjali Verma [c], Yaning Yu [d], Bin Wang [d], Peng Jiang [a,*], Hang Zhao [a], Xin Xin [a], M.A. Subramanian [c]

[a] Department of Inorganic Nonmetallic Materials, School of Materials Science and Engineering, University of Science and Technology Beijing, Beijing 100083, China
[b] School of Chemistry, Institute of Science, Suranaree University of Technology, Nakhon Ratchasima, 30000 Thailand
[c] Department of Chemistry, Oregon State University, Corvallis, OR 97330, USA
[d] Department of Chemistry, School of Science, Tianjin Chengjian University, Tianjin 300384, China

ARTICLE INFO

ABSTRACT

Magnetoplumbite-type oxides display various properties and find applications in multiple fields. In this study, a novel magnetoplumbite-type solid solution $BaZn_{6-x}Ni_xTi_6O_{19}$ ($0 \leq x \leq 4$) with vivid green color was synthesized through a high-temperature solid-phase method for the first time. The as-synthesized $BaZn_{6-x}Ni_xTi_6O_{19}$ solid solution crystallizes in the space group of P6$_3$/*mmc*. The solid solution exhibits excellent green property, and its color is adjustable with increasing doping levels of Ni^{2+}. The depth of color originates from the content and position of Ni^{2+} in the solid solution. $BaZn_{6-x}Ni_xTi_6O_{19}$ is suitable for PMMA (Polymethyl methacrylate) pigment and hydrophobic coating. Colored PMMA containing $BaZn_{6-x}Ni_xTi_6O_{19}$ exhibits vibrant colors with high saturation, showing excellent application potential. The hydrophobic coating compounded with $BaZn_{6-x}Ni_xTi_6O_{19}$ exhibits near-superhydrophobic properties and demonstrates excellent self-cleaning effects under simulated natural environmental conditions.

1. Introduction

Magnetoplumbite-type oxides have attracted widespread attention in various fields due to their excellent properties and structural characteristics. With a general formula of $AB_{12}O_{19}$ in hexagonal structure, the magnetoplumbite-type oxide is a widely researched oxide family. Among them, $BaFe_{12}O_{19}$ has emerged as a prominent choice for the base materials of permanent magnets due to chemical, thermal stability and affordable expense [1]. Lanthanum magnetoplumbites $LnMgAl_{11}O_{19}$ (Ln = La, Nd, Sm, Gd) are used in thermal barrier coatings because of their high melting point, thermal expansion, and low thermal conductivity [2]. In addition to excellent properties, magnetoplumbite-type structure is also rich in doping sites for rare earth and transition metals, resulted in their wide applications in fluorescent materials [3]. These abundant doping sites in magnetoplumbite-type structure also widen their potential applications to pigments. Pigments based on $CaAl_{12}O_{19}$, $(Sr, Ca)Fe_{12}O_{19}$, and $BaMg_6Ti_6O_{19}$ magnetoplumbite structure exhibit excellent color properties [4–9].

The magnetoplumbite-type structure is composed of a triangular bipyramidal layer (R block) and a spinel layer (S block), and the R* block and S* block are obtained by rotating the R block and S block 180° along c-axis. So the crystal structure of the magnetoplumbite-type can be expressed as RSR*S* [10]. The alternating arrangement of cubic layers and hexagonal layers in magnetoplumbite-type structure determines its hexagonal symmetry in the crystal structure. Fig. 1 shows the detailed magnetoplumbite-type structure with five different B crystallographic sites, namely three different octahedron (B1 and B5 are edge-shared octahedron, and B4 is a face-shared octahedron), tetrahedron (B3) and trigonal bipyramid (B2) [8].

With special crystal features and wide applications, discovering new compounds in the magnetoplumbite-type family is always attractive. $BaZn_6Ti_6O_{19}$, which is mentioned in few reference, has not been synthesized and analyzed yet [11,12]. According to the reference, Zn^{2+}-Ti^{4+} co-doping in $BaFe_{12}O_{19}$ is possible. However, the compound of $BaZn_6Ti_6O_{19}$ is difficult to synthesize. In this work, Ni^{2+} is introduced into $BaZn_6Ti_6O_{19}$ to stabilize the magnetoplumbite-type structure

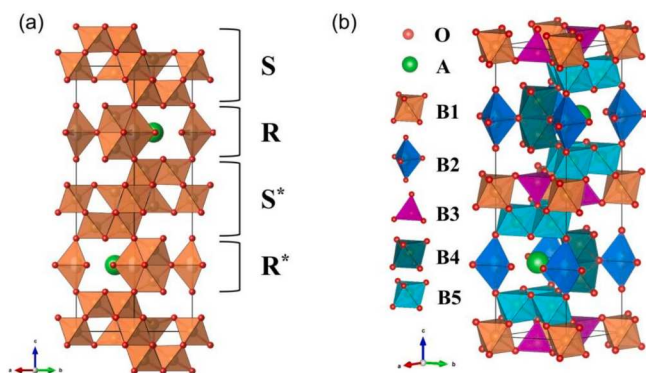* Corresponding author.
  E-mail address: jiangp@ustb.edu.cn (P. Jiang).

Fig. 1. The crystal structure of magnetoplumbite-type oxide.

through simple solid state synthesis method. The synthesized $BaZn_{6-x}Ni_xTi_6O_{19}$ demonstrates exceptional color properties and, as an MMOP (Mixed Metal Oxide Pigments), is a highly inert compound that do not contain any bioavailable or degradable substances [13,14]. This makes it a very promising non-toxic, environmentally friendly green pigment. The structure, color origin, and optical properties were analyzed by X-ray diffraction analysis, X-ray photoelectron spectroscopy, and UV-Vis-NIR absorbance spectrum. Additionally, the coloring ability of $BaZn_{6-x}Ni_xTi_6O_{19}$ was explored through its combination with PMMA (Polymethyl methacrylate). The pigment was mixed with organic silicon resin and precipitated SiO_2 to prepare green self-cleaning coating and the hydrophobic properties of the coating were investigated.

2. Experimental

2.1. Sample preparation

The $BaZn_{6-x}Ni_xTi_6O_{19}$ ($0 \leq x \leq 4$) samples were synthesized from $BaCO_3$ (99.95 % purity, Aladdin, China), ZnO (99.99 % purity, Aladdin, China), NiO (99.0 % purity, Aladdin, China) and TiO_2 (98.0 % purity, Sinopharm Chemical Reagent, China) mixtures using conventional high-temperature solid-state synthesis. After weighing the raw materials according to a specific measurement ratio, the raw materials were put into the agate mortar to mix for 20 min. Then, the mixtures were put into the mold for 3 min under 10 MPa to obtain sheet raw materials. The sheet raw materials were sintered at 1150℃ for 6 h. Later, the sintered samples were ground again and pressed into pellets. And the pellets were sintered at 1300℃ for 18 h.

The synthesized $BaZn_5NiTi_6O_{19}$ powder was dispersed in acetic acid (pH = 3) and ammonia solution (pH = 12) for acid-alkali resistance tests. The samples were soaked at room temperature for 12 h, then washed with deionized water until the pH value reached 7. Finally, the pigment powder was dried in an oven at 60 °C to remove any residual moisture.

2.2. Preparation of colored PMMA

The $BaZn_{6-x}Ni_xTi_6O_{19}$ ($0 \leq x \leq 4$) samples were added to the ball mill jar to grind via a bench-top planetary automatic ball mill (MSK-SFM-1) at 300 rpm for 10 h. BPO (benzoyl peroxide, 10 mg, AR purity, Aladdin, China) was dissolved in MMA (methyl methacrylate, 10.0 mL, 99.0 % purity, Aladdin, China) in a glass flask. When the BPO was completely dissolved, the ground samples were added to the glass flask. Then, the mixture was magnetically stirred at 85℃ until the mixture closed glycerin. Finally, the mixture was transferred to a glass tube, cured at 50℃ for 24 h, and reacted at 100℃ for 1 h to obtain colored PMMA.

2.3. Preparation of green hydrophobic coating

The organic silicon resin (Damao Chemical Reagents Factory Co., Ltd, China), $BaZn_2Ni_4Ti_6O_{19}$ green pigment and precipitated SiO_2 were thoroughly ground in a mortar. The mixture was then placed in an oven at 70 °C and dried for 20 min. This process was repeated 3 to 5 times. After cooling to room temperature, the slurry was transferred to a glass bottle. Then tetrachloroethylene (AR, Tianjin Ruijinte Chemicals Co., Ltd, China), fumed SiO_2, and of PF-550 (solvent-based fluororesin, Anhui Zhong En Chemical Co., Ltd, China) were added to the slurry, and it was stirred for 1-2 h until there are no noticeable large particles. Finally, phenyl tributyl oxime silane (AR, Tianjin Jiangtian Chemical Technology Co., Ltd, China), 3-aminopropyltriethoxysilane (98 %, Damao Chemical Reagents Factory Co., Ltd, China), and dibutyltin dilaurate (AR, Tianjin Jiangtian Chemical Technology Co., Ltd, China) were added to the slurry and stirred for 15-30 min.

Two 5 cm × 5 cm ordinary glass plates were selected and wiped clean with anhydrous ethanol. RTV (hydrophobic coating, Tianjin Dalv Power Technology Co., Ltd, China) was applied to one of the cleaned glass plates. After the RTV-coated glass plate dried on the surface, the previously prepared mixed slurry was evenly sprayed onto both the RTV-coated and uncoated glass plates using a spray gun.

2.4. Characterization

The identification of crystalline phases in the samples was conducted using X-ray diffraction (XRD) with a Rigaku Ultima IV X-ray diffractometer. The instrument utilized Cu Kα ($\lambda = 1.5406$ Å), operating at 40 kV and 40 mA, and radiation in the 2θ range of $10 - 90°$ with a scanning speed of 5°/min and a step size of 0.02°. Crystal structures were refined by the Rietveld method using the GSAS-EXPGUI software [15,16].

The oxidation states of Ni in $BaZn_6Ti_6O_{19}$ were obtained by X-ray photoelectron spectroscopy (XPS, Thermo Scientific K-Alpha).

The $L*a*b*$ color parameters of sample powders and PMMA surfaces were analyzed using the X-Rite Ci7600 benchtop spectrophotometer. In the context of the CIE $L*a*b*$ system, $L*$ corresponds to brightness, $a*$ represents the hue from green to red, and $b*$ denotes the hue from blue to yellow.

UV-Vis-NIR absorbance spectra for sample powders and PMMA were recorded within the wavelength range of 200 nm to 2500 nm at room temperature using a UV-Vis-NIR spectrophotometer (Hitachi UH4150). Barium sulfate ($BaSO_4$) served as the white reference.

The thermal stability of samples was measured by a HITACHI STA200 simultaneous thermal analyzer with a heating rate of 10 °C/min from room temperature to 600 °C at air atmosphere.

2.5. Computational details

All calculations were carried out using the spin-polarized density functional theory (DFT) method, as implemented in Vienna ab initio simulation package (VASP 6) [17,18]. To describe the electron–ion interaction, the frozen-core projector augmented wave (PAW) method was employed [19]. The exchange–correlation term was approximated using the generalized gradient approximation (GGA) with Perdew-Burke-Ernzerhof (PBE) functional [20]. The valence electrons of Ba 5 s 5p 6 s, Zn 3d 4p, Ni 3d 4 s, Ti 3d 4 s, and O 2 s 2p were expanded in a plane wave basis with a kinetic energy cutoff of 500 eV. The DFT$+U$ method was employed with on-site correction of 3.9 eV ($U_{eff} = 3.9$ eV) and 6.4 eV ($U_{eff} = 6.4$ eV) for Ti 3d and Ni 3d electrons, respectively, as used for their oxides reported in previous studies [21–23]. To obtain the doping concentrations according to the experimental results, we constructed a 2 x 2 x 1 supercell model of $BaZn_6Ti_6O_{19}$ with lattice parameters $a = 11.93$ Å, $b = 5.99$ Å, $c = 23.64$ Å. The Ni^{2+} doped systems can be obtained by replacing Zn atoms with Ni atoms to yield $BaZn_4Ni_2Ti_6O_{19}$ and $BaZn_2Ni_4Ti_6O_{19}$. The Brillouin zone sampling were carried out using the Monkhorst–Pack scheme [24] with k-point of 4 x 5 x 2

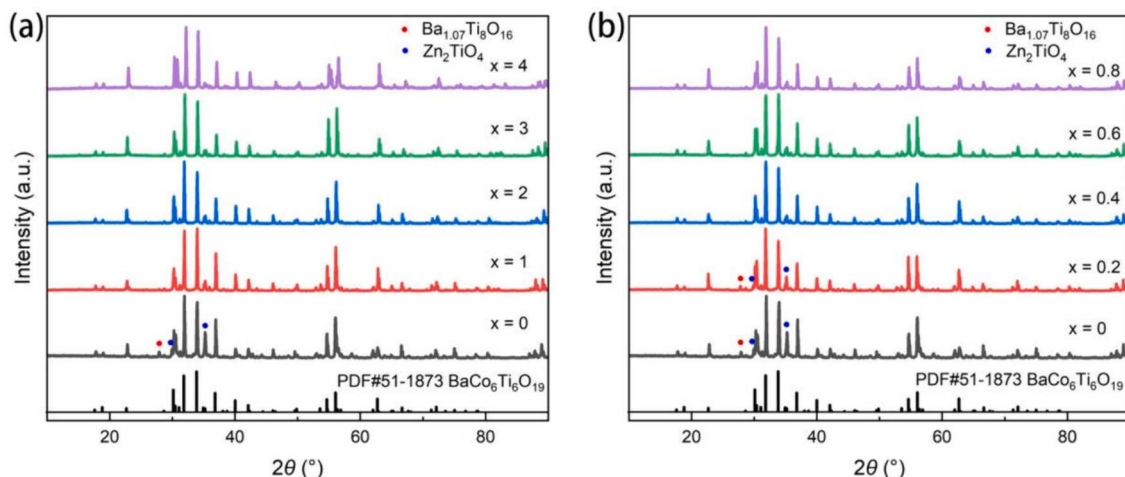**Fig. 2.** The XRD patterns of BaZn$_{6-x}$Ti$_6$Ni$_x$O$_{19}$ (a) ($0 \leq x \leq 5$) and (b) ($0 \leq x \leq 0.8$).

Fig. 3. (a) Rietveld refinement of the XRD pattern for BaZn$_4$Ti$_6$Ni$_2$O$_{19}$ and (b) refined crystal structure of BaZn$_4$Ti$_6$Ni$_2$O$_{19}$.

for structural optimization, while a denser k-point of 7 x 8 x 2 was used for computations of electronic density of states (DOS). Forces and energy convergence were set to 0.02 eV/Å and 10^{-6} eV, respectively.

3. Results and discussion

The as-synthesized BaZn$_{6-x}$Ni$_x$Ti$_6$O$_{19}$ belongs to M−type magneto-plumbite structure which could be indexed to the space group of BaCo$_6$Ti$_6$O$_{19}$ (PDF#51–1873, P6$_3$/mmc). Fig. 2a shows XRD patterns of BaZn$_{6-x}$Ni$_x$Ti$_6$O$_{19}$ (x = 0, 1, 2, 3, 4, and 5). It can be seen from Fig. 2a that characteristic peak of the impurities Ba$_{1.07}$Ti$_8$O$_{16}$ (at 27.80°) and Zn$_2$TiO$_4$ (at 29.77° and 35.15°) are observed in BaZn$_6$Ti$_6$O$_{19}$ without Ni^{2+} doping. The Fig. 2b is the XRD patterns of BaZn$_{6-x}$Ni$_x$Ti$_6$O$_{19}$ ($0 \leq x \leq 0.8$). The impurities Ba$_{1.07}$Ti$_8$O$_{16}$ and Zn$_2$TiO$_4$ also appear in BaZn$_{5.8}$Ni$_{0.2}$Ti$_6$O$_{19}$. As the Ni^{2+} doping amount increases, the intensity of the impurity characteristic peaks decreases until full disappearance. BaZn$_{6-x}$Ni$_x$Ti$_6$O$_{19}$ samples ($0.2 \leq x \leq 4$) show single phase indexed to the space group of P6$_3$/mmc. When the Ni^{2+} doping amount excess x = 4, new impurities appear.

As illustrated from the Rietveld refinement results in Fig. 3b and Table 1, for sample with lower Ni^{2+} doping concentration, the tetrahedron positions (4f1) and the trigonal bipyramidal positions (4e) are entirely occupied by Zn^{2+}. The 2a site is allocated to Ti^{4+} while the 4f2 sites are jointly occupied by Zn^{2+} and Ti^{4+}. Ni^{2+} is introduced in the 12 k

site, sharing with Ti^{4+}. Generally, Zn^{2+} demonstrates a preference for entering tetrahedron positions, while Ni^{2+} and Ti^{4+} exhibit a robust tendency to occupy octahedron positions (for detailed structure, refer to Supplementary CIF 1) [25–30]. The phenomenon can be explained by the stability of tetrahedral covalent bonds of Zn^{2+}. The energies of nd and (n + 1)s orbitals of Zn^{2+} almost reach the same, so covalent tetrahedral bonds are easily formed. The covalent bonds are shorter than ionic bonds. Consequently, Zn^{2+} is more readily accommodated in tetrahedron positions than other ions [31]. Ni^{2+} prefer to occupy octahedron positions due to their d^8 configuration and the crystal field stablization energy of octahedron site [32].

In Fig. 4b and Table 2, upon increasing the doping concentration of Ni^{2+}, Ni^{2+} will take place of Zn^{2+} in the 4f1 octahedron site. Ti^{4+} starts to enter the 4e site. The 2a, 4f2, and 12 k sites are concurrently occupied by both Ni^{2+} and Ti^{4+}. The electronegativity can serve as a predictive indicator for Ni^{2+} and Ti^{4+} ion positions (for detailed structure, refer to Supplementary CIF 2). Ions with higher electronegativity are predisposed to occupy octahedral positions. The electronegativities of Ni and Ti atoms are 1.92 and 1.54, respectively [32]. Consequently, Ni^{2+} exhibit a tendency to occupy octahedral positions. According to previous study, when Ni^{2+} occupies the octahedron positions, Ti^{4+} ions may occupy the 4f1 or 4e sites. In these samples, as the concentration of Zn^{2+} decreases, Ti^{4+} ions occupy the 4e positions. Despite the general inclination of Ni^{2+} taking the octahedron positions, it is noteworthy that in

Table 1
Values of atomic lattice parameters, positional, coordinates, occupancy and thermal parameters determined from Rietveld refinement of XRD pattern of $BaZn_4Ti_6Ni_2O_{19}$.

$a(Å)$	$b(Å)$	$c(Å)$	$α(°)$	$β(°)$	$γ(°)$	volume $(Å^3)$
5.9005 (3)	5.9005 (3)	23.433(1)	90	90	120	706.55 (9)
atom	site	occupancy	x	y	z	Uiso $(Å^2)$
Ba1	2d	1	0.6667	0.3333	0.2500	0.0152
Ti1	2a	1	0.0000	0.0000	0.0000	0.0034 (7)
Zn2	4f	1	0.3333	0.6667	0.0257 (4)	0.0141 (8)
Zn3	4f	0.5	0.3333	0.6667	0.1912 (6)	0.0305 (5)
Ti3	4f	0.5	0.3333	0.6667	0.1912 (6)	0.0305 (5)
Zn4	4e	0.5	0.0000	0.0000	0.2599 (7)	0.0569 (8)
Ti5	12 k	0.6667	0.1694 (2)	0.3389 (5)	0.8946 (1)	0.0181 (2)
Ni5	12 k	0.3333	0.1694 (2)	0.3389 (5)	0.8946 (1)	0.0181 (2)
O1	4e	1	0.0000	0.0000	0.1389 (5)	0.0176 (6)
O2	4f	1	0.3333	0.6667	−0.0638 (9)	0.0459 (2)
O3	6 h	1	0.1815 (1)	0.3630 (3)	0.2500	0.0438 (4)
O4	12 k	1	0.1543 (7)	0.3086 (5)	0.0516 (7)	0.0265 (5)
O5	12 k	1	0.4994 (1)	−0.0010 (8)	0.1497 (4)	0.0189 (2)

certain compounds, Ni exhibits a dual propensity, occupying both tetrahedroal and octahedral positions, such as in the cases of $CaAl_{12-2x}Ni_xTi_xO_{19}$ and $Ca_{1-x}La_xAl_{12-x}Ni_xO_{19}$ [6,33]. In $BaZn_{6-x}Ni_xTi_6O_{19}$, the extensive substitution of Zn^{2+} by Ni^{2+} results in a minor introduction of Ni^{2+} into the 4f1 site. The validation of this phenomenon is further corroborated by subsequent optical analyses [6,33–35].

The ionic radii of Zn^{2+}, Ni^{2+}, and Ti^{4+} ions are 0.74, 0.63, and 0.60 Å, respectively [27]. The reduction of lattice parameter and unit cell volume can be attributed to the substitution of Ni^{2+} in place of the Zn^{2+} ions.

In order to determine the oxidation state of Ni in $BaZn_{6-x}Ni_xTi_6O_{19}$, XPS analysis was performed. Fig. 5a is XPS full scan spectrum of sample $BaZn_5NiTi_6O_{19}$, in which the absorption peaks of O, Zn, Ti, Ni, Ba and C elements are detected. As can be seen from Fig. 5b, the binding energy of

the $Ni2p_{3/2}$ is 855.44 eV and corresponding satellite peak is located at 861.36 eV. The binding energy of the $Ni2p_{1/2}$ is 872.71 eV and corresponding satellite peak locates at 879.72 eV. The value of above four binding energies in $BaZn_{6-x}Ni_xTi_6O_{19}$ are similar to the binding energies of Ni^{2+} in NiO/SnO_2 nanocomposites, $Ni_{0.15}Mg_xAl_{2(0.85-x)}Ti_{1.15+x}O_5$, $Al_{1.85}Ni_{0.15}TiO_5$ and $Sr_{1-x}Ni_xAl_{11.2+x}Ni_{0.8-x}O_{19-δ}$ showed in Table 3. Therefore, the $Ni2p_{3/2}$, $Ni2p_{3/2}$ satellite, $Ni2p_{1/2}$ and $Ni2p_{1/2}$ satellite in the sample are all the characteristic peaks of Ni^{2+}.

To verify the chemical stability of the $BaZn_{6-x}Ni_xTi_6O_{19}$, the $BaZn_5NiTi_6O_{19}$ pigment was dispersed in acetic acid (pH = 3) and ammonia (pH = 12) for acid-alkali resistance tests. Before and after the tests, there was no significant change in the appearance color of the samples (as shown in Fig. 6).

From the analysis of the XRD patterns (as shown in Fig. 6) of $BaZn_5NiTi_6O_{19}$ before and after the acid-alkali resistance test, the peak positions remain unchanged, while the peak shapes exhibit certain variations. This indicates that the crystal structure of the pigment has not undergone significant changes, although its microstructure or crystal defects may have been altered. Therefore, it can be concluded that the sample demonstrates satisfied structural stability.

At the same time, the color coordinates of the sample after the acid-base test were compared with those of the initial sample. Table 4 lists the $L*a*b*$ values and $ΔE*$ (total color difference of the sample). When $ΔE* ≤ 5$, the pigment is considered to exhibit excellent stability [40]. However, since the $ΔE*$ of the sample is slightly greater than 5, and considering the XRD patterns, it can be concluded that the sample is not highly stable.

According to the UV-Vis-NIR spectrum of the samples (Fig. 7a), when Ni^{2+} is at low doping levels, three distinct absorption peaks are found in the near-infrared region, the red–orange region, and the blue-violet region. These spectral characteristics are consistent with cases such as (Ni, $Mg)_2TiO_4$, $BaNiTi_7O_{16}$ and $Ni_{0.1}W_{0.1}Ti_{0.8}O_2$, in which Ni^{2+} is situated in the octahedral ligand field [41–44].

The positions of Ni^{2+} are verified by analyzing Tanabe-Sugano diagrams (Fig. 7b) of d^8 configuration. Regarding Ni^{2+} in a octahedral ligand field, the spin-allowed transitions are:

$$v_1 = {}^3A_{2g}({}^3F) → {}^3T_{2g}({}^3F) \tag{1}$$

$$v_2 = {}^3A_{2g}({}^3F) → {}^3T_{1g}({}^3F) \tag{2}$$

$$v_3 = {}^3A_{2g}({}^3F) → {}^3T_{1g}({}^3P) \tag{3}$$

By observing the spectrum in Fig. 7a, in the ultraviolet and infrared regions, two broad absorption bands are located at 360 nm (27778 cm^{-1}) and 1185 nm (8439 cm^{-1}), corresponding to ${}^3A_{2g}({}^3F) → {}^3T_{1g}({}^3P)$
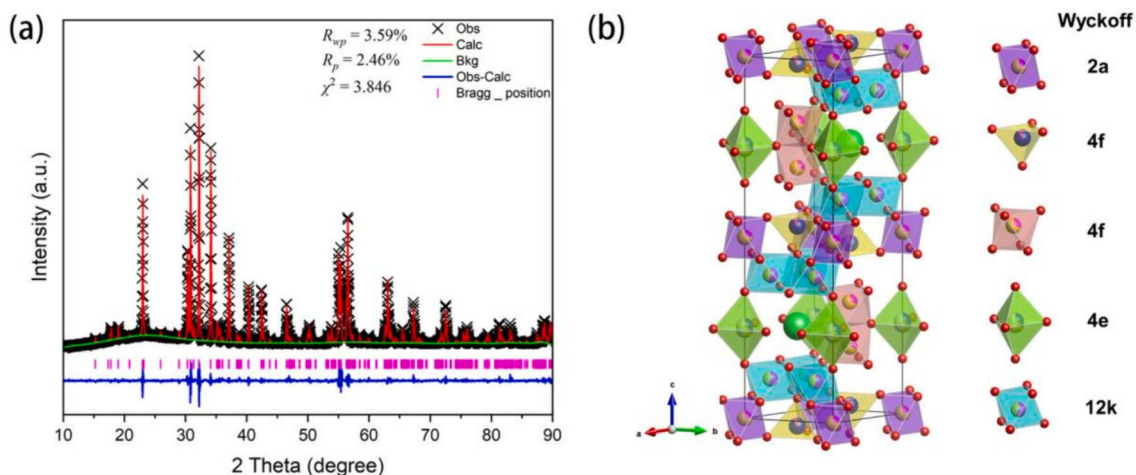

Fig. 4. Rietveld refinement of the XRD pattern for (a) $BaZn_2Ti_6Ni_4O_{19}$ and refined crystal structure of (b) $BaZn_2Ti_6Ni_4O_{19}$.

Table 2
Values of atomic lattice parameters, positional, coordinates, occupancy and thermal parameters determined from Rietveld refinement of XRD pattern of BaZn$_2$Ti$_6$Ni$_4$O$_{19}$.

a(Å)	b(Å)	c(Å)	α(°)	β(°)	γ(°)	volume (Å^3)
5.8961 (5)	5.8961 (5)	23.233(7)	90	90	120	699.45 (6)
atom	site	occupancy	x	y	z	Uiso(Å^2)
Ba1	2d	1	0.6667	0.3333	0.2500	0.0108 (6)
Ni1	2a	0.2280(3)	0.0000	0.0000	0.0000	0.0126 (5)
Ti1	2a	0.7720(6)	0.0000	0.0000	0.0000	0.0126 (5)
Zn2	4f	0.8956(8)	0.3333	0.6667	0.0262 (1)	0.0233 (7)
Ni2	4f	0.1044(1)	0.3333	0.6667	0.0262 (1)	0.0233 (7)
Ni3	4f	0.2994(5)	0.3333	0.6667	0.1877 (5)	0.0161 (5)
Ti3	4f	0.7006(4)	0.3333	0.6667	0.1877 (5)	0.0161 (5)
Zn4	4e	0.3114(6)	0.0000	0.0000	0.2459 (9)	0.0384 (6)
Ti4	4e	0.1886(3)	0.0000	0.0000	0.2459 (9)	0.0384 (6)
Ni5	12 k	0.5425(1)	0.1626 (4)	0.3253 (8)	0.8935	0.0033
Ti5	12 k	0.4575(8)	0.1626 (4)	0.3253 (8)	0.8935	0.0033
O1	4e	1	0.0000	0.0000	0.1502 (3)	0.0154 (3)
O2	4f	1	0.3333	0.6667	−0.0512 (1)	0.0030
O3	6 h	1	0.1990 (6)	0.3979 (3)	0.2500	0.0020 (7)
O4	12 k	1	0.1411 (6)	0.2821 (2)	0.0532 (1)	0.0509 (9)
O5	12 k	1	0.5049 (2)	0.0099 (6)	0.1479 (4)	0.0321 (4)

Table 3
The binding energy of Ni2p$_{3/2}$, Ni2p$_{3/2}$ satellite, Ni2p$_{1/2}$ and Ni2p$_{1/2}$ satellite in Ni-containing materials.

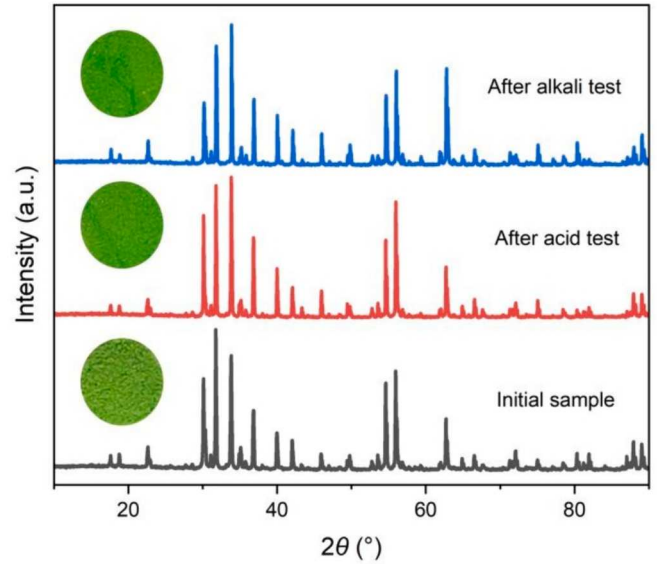| Binding energy (eV)	Ni2p$_{3/2}$	Ni2p$_{3/2}$ satellite	Ni2p$_{1/2}$	Ni2p$_{1/2}$ satellite	Ref.
NiO/SnO$_2$ nanocomposites	855.4	860.4	873.2	879.5	[36]
Ni$_{0.15}$Mg$_x$Al$_2$$_{(0.85-x)}Ti_{1.15+x}O_5$	856.52	862.39	874.02	880.38	[37]
Al$_{1.85}$Ni$_{0.15}$TiO$_5$	855.29	861.17	872.86	879.12	[38]
Sr$_{1-x}$Ni$_x$Al$_{11.2+x}$Ni$_{0.8-x}$O$_{19-\delta}$	855.9	862	873.5	880	[39]

Fig. 6. XRD pattern and digital photos of BaZn$_5$Ti$_6$NiO$_{19}$ before and after the acid-alkali resistance test.

Table 4
$L^*a^*b^*$ values and total color difference (ΔE^*) after acid-alkali resistance test.

Sample	L^*	a^*	b^*	ΔE^*
Initial state	79.33	−19.64	35.10	
Acid testing	75.82	−22.17	38.01	5.21
Alkaline testing	74.98	−22.86	38.45	6.37

$\Delta E^* = [(\Delta L^*)^2 + (\Delta a^*)^2 + (\Delta b^*)^2]^{1/2}$

and $^3A_{2g}$ (^{3}F) → $^3T_{2g}$ (^{3}F), respectively. At 654 nm (15291 cm^{-1}), a broad absorption band corresponding to $^3A_{2g}$ (^{3}F) → $^3T_{1g}$ (^{3}F) is observed. The ν_1, ν_2 and ν_3 can be used to calculate 10Dq and B values in the case of the 3d^8 octahedral configuration [38,45,46].

$$\nu_1 = 10Dq = 8439 \, \text{cm}^{-1} \tag{4}$$

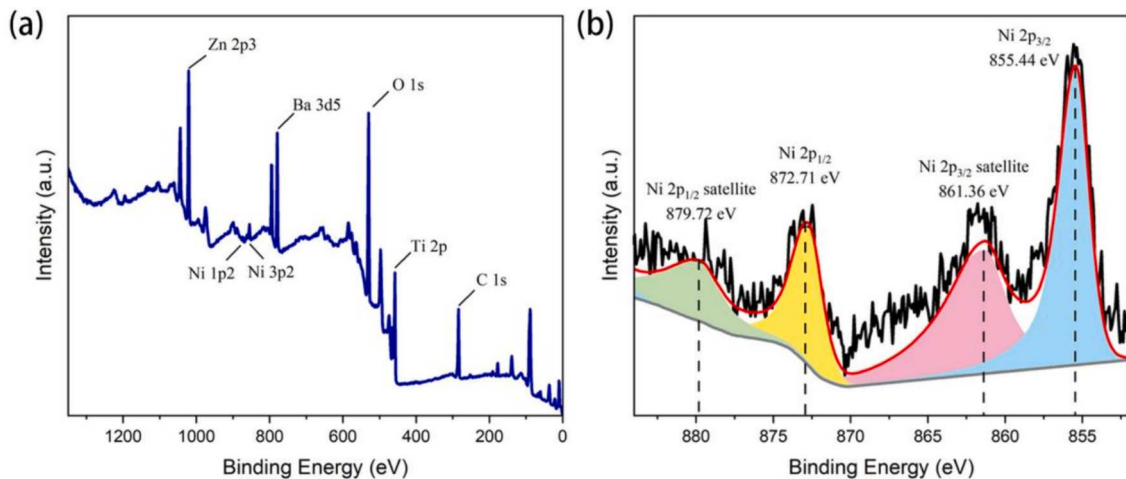$$\nu_2 = 7.5B + 15Dq - 0.5[(9B - 10Dq)^2 + 144B^2]^{0.5} = 15291 \, \text{cm}^{-1} \tag{5}$$

Fig. 5. (a) XPS full scan spectrum and (b) Ni 2p fine spectrum of sample BaZn$_5$NiTi$_6$O$_{19}$.
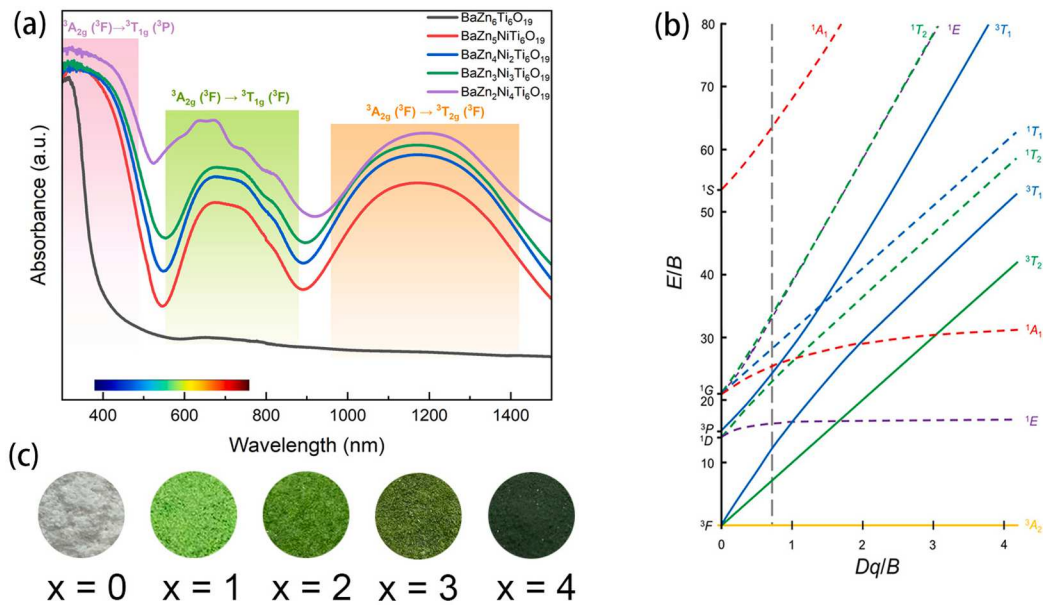
Fig. 7. (a) UV-Vis-NIR absorbance spectra (b) Tanabe-Sugano diagram and (c) digital photos of $BaZn_{6-x}Ni_xTi_6O_{19}$ powders.

$$v_3 = 7.5B + 15Dq - 0.5[(9B - 10Dq)^2 + 144B^2]^{0.5} = 27778\,cm^{-1} \quad (6)$$

All three bands are observed. The following equations can be used to calculate the parameters $10Dq$ and B.

$$10Dq = v_1 \quad (7)$$

$$B = (v_2 + v_3 - 3v_1)/15 \quad (8)$$

Based on these equations, the B value is determined to be $1183\,cm^{-1}$, the Dq value is $844\,cm^{-1}$, and the Dq/B value is 0.713. In Fig. 7b, the positional relationship of each absorption band is compared through the value of E/B. After comparison and calculation, it is concluded that the absorption band in the Tanabe-Sugano diagram is entirely consistent with the spectral characteristics of the absorption band in the sample spectrum. Thus, it is confirmed that Ni^{2+} exists in the octahedron crystal field environment, which is consistent with the Rietveld refinement stated in previous part. Thus, the three peaks in Fig. 7a correspond to the three spin-allowed transitions, $^3A_{2g}$ $(^3F) \to {}^3T_{2g}$ (^3F), $^3A_{2g}$ $(^3F) \to {}^3T_{1g}$ (^3F) and $^3A_{2g}$ $(^3F) \to {}^3T_{1g}$ (^3P). Transitions $^3A_{2g}$ $(^3F) \to {}^3T_{1g}$ (^3F) and $^3A_{2g}$ $(^3F) \to {}^3T_{1g}$ (^3P) are located in the visible region, which are responsible for the pigments' color. The absorption peaks around 750 nm are caused

by forbidden transitions [41,47]. The $^3A_{2g}$ $(^3F) \to {}^3T_{1g}$ (^3P) transition and the absorption band of the matrix at 266 nm form a broad absorption band in the ultraviolet–visible region.

Fig. 7a shows that $BaZn_2Ti_6Ni_4O_{19}$ exhibits a shoulder peak at 600 nm. The particular absorption peak closely resembles the characteristic absorption peak of Ni^{2+} in tetrahedral coordination. The absorption peak at 600 nm is a collection of two spin-allowed transitions and two spin-forbidden transitions from the d-d transition of Ni^{2+} within the tetrahedral coordination [6].

The UV-Vis-NIR absorbance spectra of the samples show the characteristic peaks of Ni^{2+} in the octahedral sites, indicating that Ni^{2+} doping in $BaZn_{6-x}Ti_6Ni_xO_{19}$ tends to preferentially occupy octahedral positions. Structural refinement reveals that Ni^{2+} initially tends to occupy the 12 k positions. As the concentration of Ni^{2+} doping increases, it then occupies the 2a and 4f2 positions. As the substitution progresses, characteristic peaks of Ni^{2+} in tetrahedral positions appear in the UV-Vis-NIR absorbance spectra, indicating that Ni^{2+} has entered the tetrahedral sites of the samples. Further refined structural information shows that when Ni^{2+} entirely replace Zn^{2+} in the octahedron site, Ni^{2+} will then enter the 4f1 tetrahedral positions in $BaZn_{6-x}Ti_6Ni_xO_{19}$.

The color of $BaZn_{6-x}Ti_6Ni_xO_{19}$ is mainly determined by Ni^{2+} in the
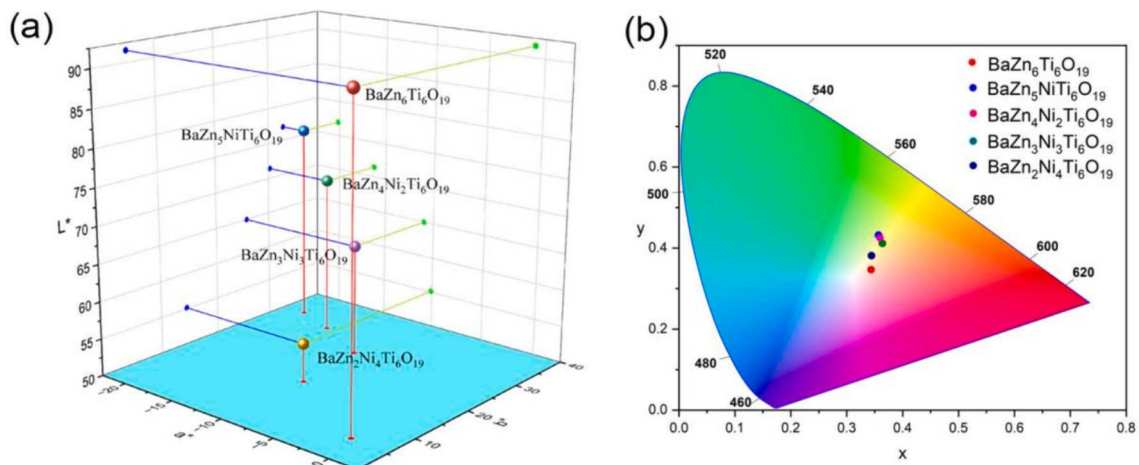

Fig. 8. (a) Color coordinates in $L*a*b*$ space and (b) chromaticity diagram of $BaZn_{6-x}Ni_xTi_6O_{19}$ powders.
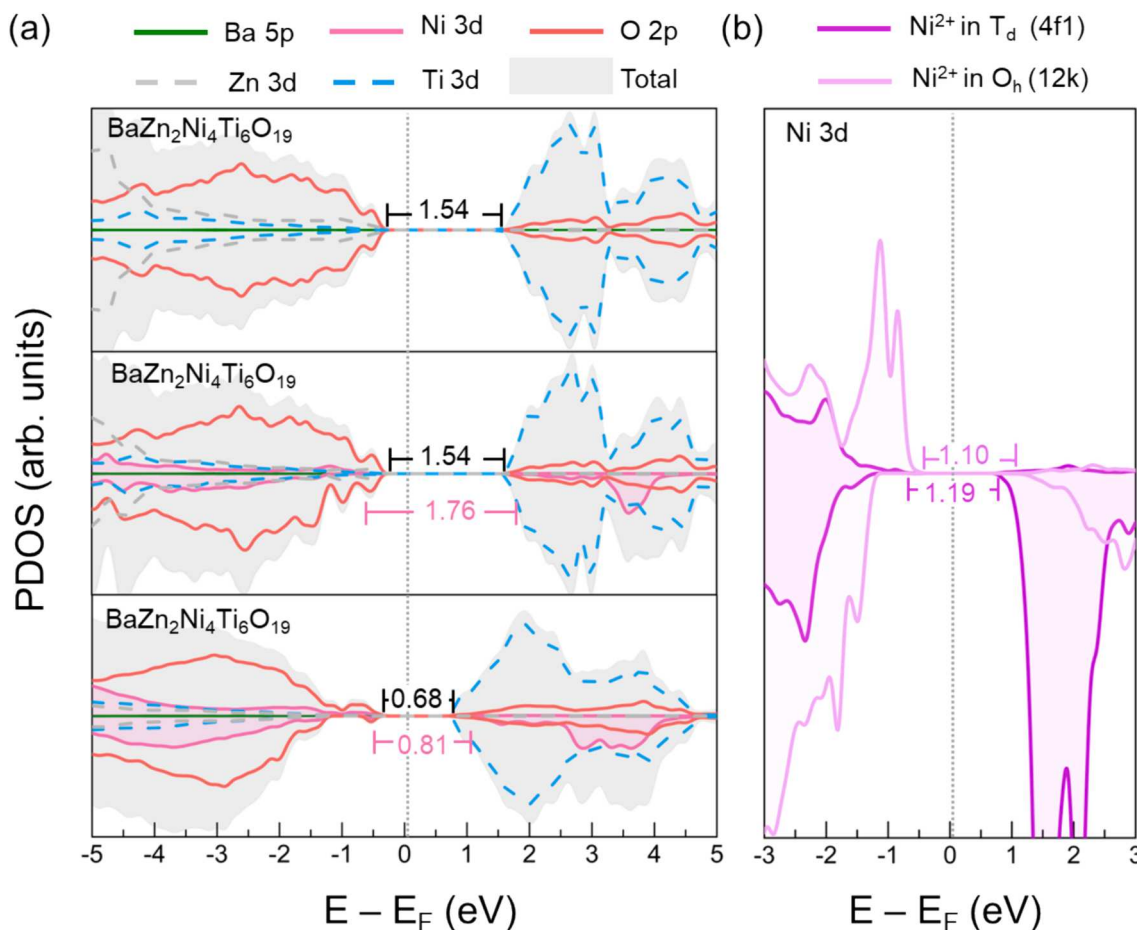
Fig. 9. Projected density of states (PDOS) of (a) $BaZn_{6-x}Ni_xTi_6O_{19}$ systems ($x = 0, 2, 4$). Labeled numbers in black and pink indicate the band gap and Ni d-d gap, respectively. (b) Comparison of Ni d-d gap in tetrahedral site and octahedral site of the $BaZn_2Ni_4Ti_6O_{19}$ system.

octahedron positions. The content of Ni^{2+} in tetrahedral sites is lower, having a relatively smaller impact on the pigments' color. From Fig. 7c, it can be seen that as the content of Ni^{2+} in octahedral sites continues to increase, the color of the pigment gradually deepens. When the doping amount x in $BaZn_{6-x}Ti_6Ni_xO_{19}$ reaches 4, Ni^{2+} begins to enter the tetrahedral sites, resulting in a decrease in absorption around 500 nm, and an increase in the blueness of the pigment, making the color even more profound.

As observed in Fig. 8a which exhibits the color coordinates of the as-synthesized samples in $L^*a^*b^*$ space, the L^* value of the samples decreases when Ni^{2+} doping amount increases, indicating the brightness of the samples gradually decreases. This trend is also indicated in the digital photos in Fig. 8c. The value of a^* gradually increases, and the b^* value gradually decreases towards 0. Changes in the a^* and b^* values are manifested as the samples chroma moving towards both blue and red shown in Fig. 8b (chromaticity diagram of the as-synthesized samples).

To better understand the color change of the samples upon doping, we employed the DFT+U method to calculate and analyze the projected density of states (PDOS) of the $BaZn_{6-x}Ni_xTi_6O_{19}$ systems ($x = 0, 2, 4$). Firstly, we explored the most stable configurations of Ni^{2+} doping at various concentrations by varying Ni^{2+} doping positions based on our Rietveld refinement of XRD pattern. We find that Ni^{2+} tends to distribute throughout the supercell in both low (12 k site) and high doping concentrations (4f1, 2a, 4f2 and 12 k site), as detailed in Supporting Information. In addition, Ni^{2+} doping leads to reduction of cell volume by 3.7 % due to the smaller ionic radius of Ni^{2+} compared to Zn^{2+} and Ti^{4+}. The calculated results are consistent with our Rietveld refinement of XRD pattern.

As shown in Fig. 9a, the calculated PDOS of $BaZn_6Ti_6O_{19}$ exhibits a

band gap of 1.54 eV. Its valence band (VB) primarily comprises O 2p states with non-negligible overlap of Zn and Ti 3d states, while the conduction band (CB) displays strong hybridization of Ti 3d and O 2p states. Doping Ni^{2+} at low concentration ($BaZn_4Ni_2Ti_6O_{19}$) introduces additional Ni 3d states at both VB and CB while the band gap remains unaffected. Nevertheless, the observed bright green color of the material could be attributed to the d-d transition of Ni 3d states at VB and CB with the gap of 1.76 eV. As the Ni^{2+} concentrations increase, the band gap reduces to 0.68 eV, which leads to the reduction of the Ni^{2+} d-d transition gap to 0.81 eV. The reduction of the band gap and Ni^{2+} d-d gap could be the origin of the darker colors of the samples with high Ni^{2+} concentrations.

Interestingly, the d-d gap of Ni^{2+} at tetrahedral site (Ni T_d, 4f1 site, 1.19 eV) is larger than d-d gap than that of Ni^{2+} at octahedral site (Ni O_h, 12 k site, 1.10 eV), as shown in Fig. 9b. The calculated results agree with the experimentally observed absorption spectra where the transition of Ni T_d exhibits absorption at lower wavelength than that of Ni O_h.

It is noteworthy that electronic structures derived from DFT+U calculations may display discrepancies in predicting band gaps due to inherent self-interaction errors in DFT. However, despite this limitation, the observed trend in band gap reduction resulting from Ni^{2+} doping offers valuable insight into the effects of varying Ni^{2+} doping concentrations, aligning well with experimental findings.

4. Analysis of PMMA optical properties

The as-synthesized $BaZn_{6-x}Ni_xTi_6O_{19}$ powders are polymerized with PMMA for potential application study. Compared to the powder samples, the L^* value of colored PMMA decreases, and the brightness
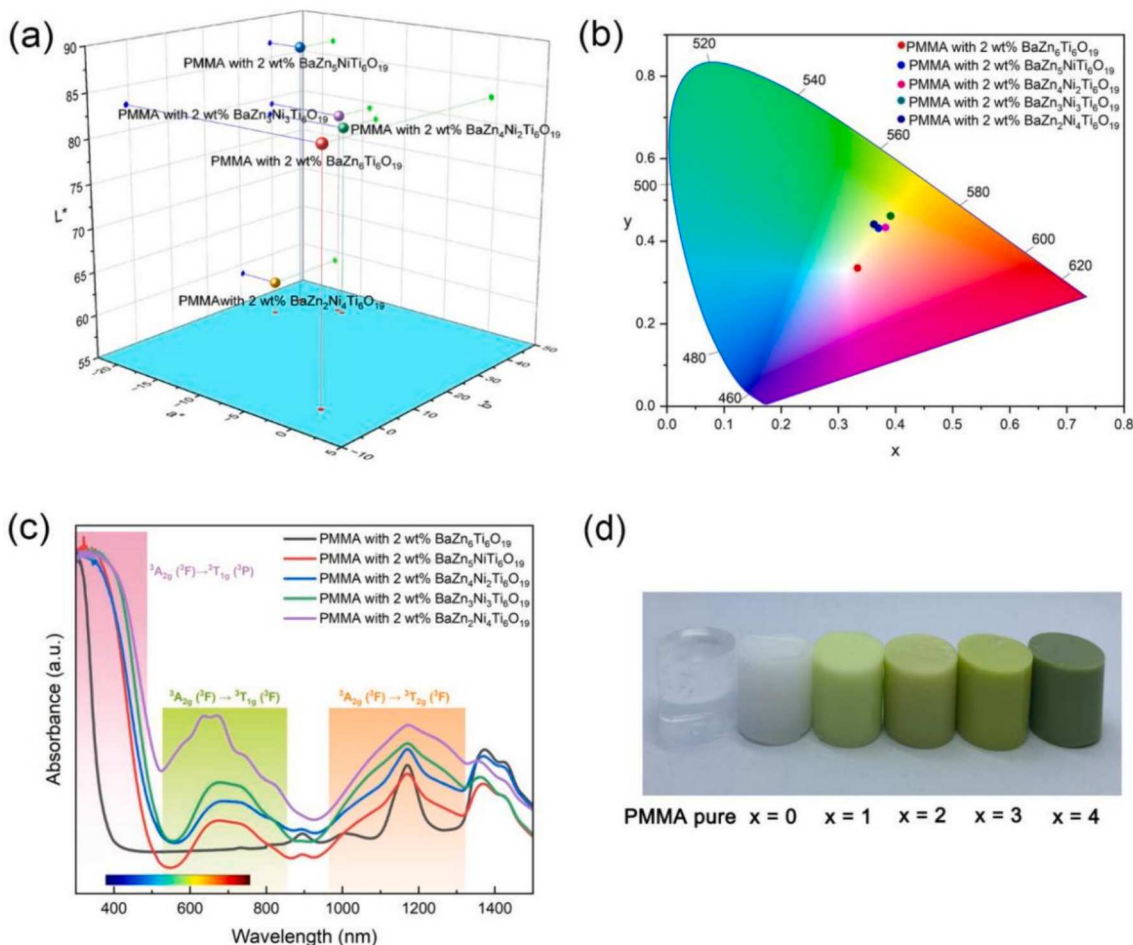
Fig. 10. (a) Color coordinates in $L^*a^*b^*$ space, (b) chromaticity diagram, (c) UV-Vis-NIR absorbance spectra and (d) digital photos of pure PMMA and colored PMMA.
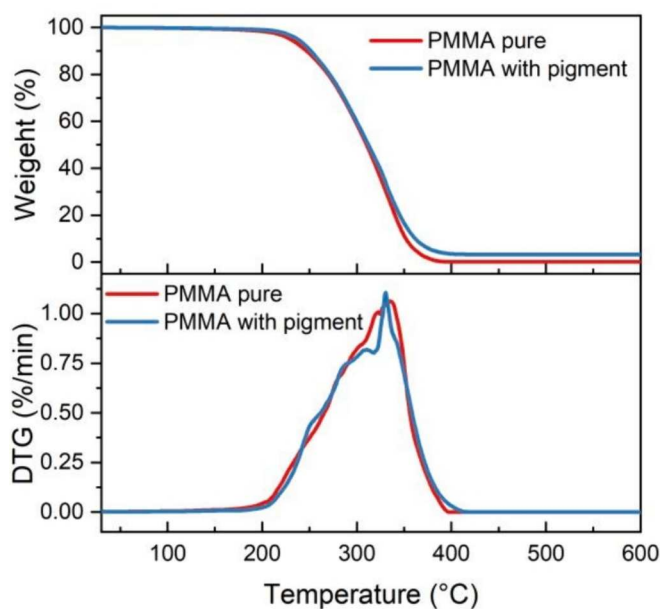

Fig. 11. TG/DTG of PMMA.

becomes darker. The elevation in the b^* value of colored PMMA enhances the yellow chroma of PMMA compared to the $BaZn_{6-x}Ni_xTi_6O_{19}$ samples, as illustrated in Fig. 10a. In Fig. 10b, the points representing the colored PMMA move up in contrast to points representing the green powder samples in Fig. 10b, and the yellow color has deepened.

Between colored PMMA and powder samples, there is no significant change in the a^* value and the green hue. As shown in Fig. 10c, the UV-Vis-NIR absorbance spectra of colored PMMA are similar to the characteristic peaks of Ni^{2+} in the octahedron and tetrahedron in the $BaZn_{6-x}Ni_xTi_6O_{19}$ powder samples. Therefore, powder samples are the color source of colored PMMA. Comparing with samples, the reflection peak of PMMA in the visible light region broadens, and the reflection in the yellow visible region is covered. As shown in Fig. 10b and d, the apparent color changes from yellow to yellow-green. The color exhibits some variances from powder samples. This is mainly due to the transparent PMMA plastic owns a different refractive index from the powder samples. The above results indicates that $BaZn_{6-x}Ni_xTi_6O_{19}$ exhibits excellent coloring properties.

To verify the effect of the pigment on the thermal stability of PMMA, TG/DTA analysis was performed on the PMMA [48]. As observed from Fig. 11, the TG/DTA curves of the two types of PMMA are similar, meaning the onset of thermal decomposition and the decomposition rates are approximately the same. The incorporation of pigments does not affect the thermal stability of PMMA.

5. Analysis of colorful hydrophobic coatings

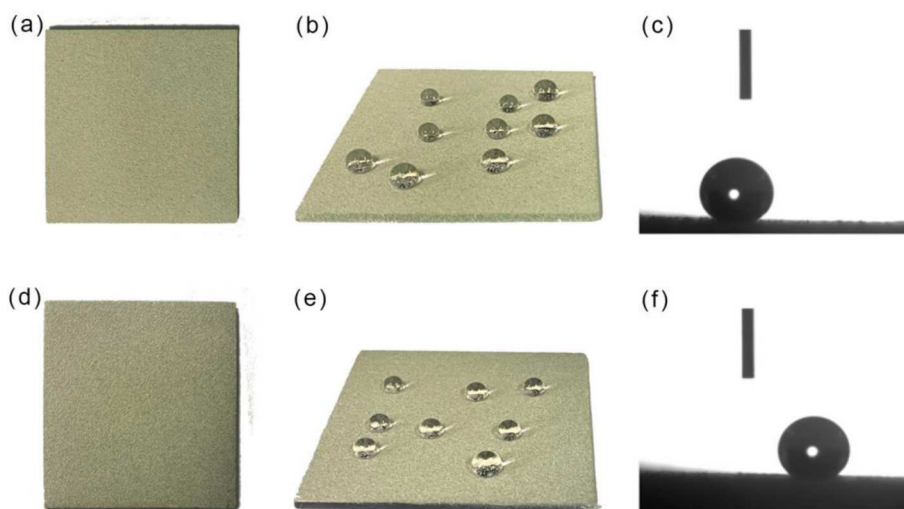Fig. 12a and b show green coatings without primer and with primer,

Fig. 12. Photos of the green coating: (a) without primer spray, (d) with primer spray; spherical water droplets on the green coating: (b) without primer spray, (e) with primer spray; and images of water droplets in contact with the hydrophobic surface: (c) without primer spray, (f) with primer spray.
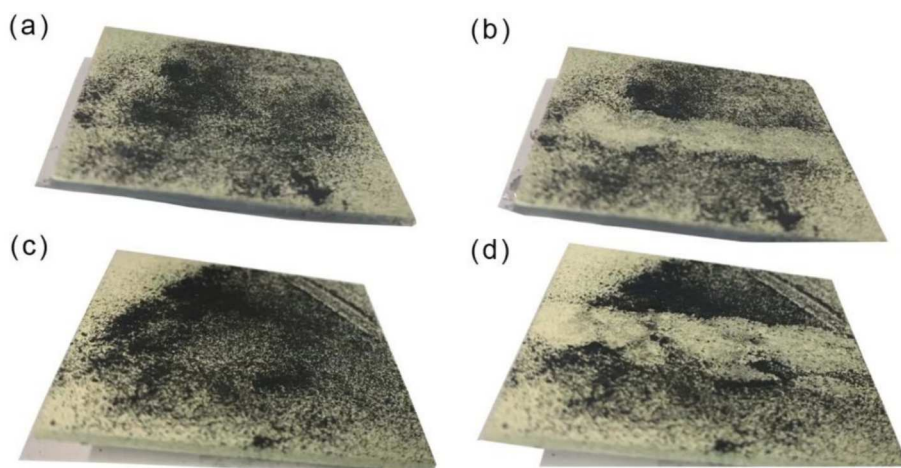

Fig. 13. The self-cleaning process of the superhydrophobic surface (a) and (b) without primer spray, (c) and (d) with primer spray.

respectively, displaying a light green coloration. In Fig. 12b and e, water droplets placed on both types of coatings remain as spherical droplets on the surface (as shown in Supplementary Video 1 and 2), indicating that both coatings exhibit hydrophobic properties. When the glass plate is tilted at 6.5°, test indicates that the green coating without primer has a CA (contact angle) and RA (rolling angle) of 146.16° and 8°, respectively (as shown in Fig. 12c and Supplementary Video 3). When the glass plate is tilted at 2°, the experiment shows that the CA and RA of the green coating with primer are 143.67° and 9° respectively. (as shown in Fig. 12f and Supplementary Video 4). Their CA are close to 150°, and RA are less than 10°, exhibiting near-superhydrophobic properties [49].

Carbon powder was sprinkled on both types of coatings, and deionized water was dropped onto the coatings using a pipette to simulate raindrops. When deionized water was dropped onto the coatings, the droplets quickly rolled off and came into contact with the carbon powder, washing away the carbon powder on the surface and leaving clean paths (Fig. 13). Therefore, we infer that under natural rainfall conditions, dust can be washed away by water droplets, achieving a self-cleaning effect [50].

6. Conclusions

The solid solution of $BaZn_{6-x}Ni_xTi_6O_{19}$ with magnetoplumbite structure has been synthesized for the first time. According to the structure refinement, Zn^{2+} occupies all of the tetrahedral and trigonal bipyramidal positions, and the partial octahedron positions. Ti^{4+} exhibits no specific positional tendency and occupies sites based on the positional advantages of other ions. Ni^{2+} tends to preferentially occupy the octahedron positions. With the elevation of Ni^{2+} doping concentration, Ni^{2+} progressively replaces Zn^{2+} at the octahedron positions. It will further replace Zn^{2+} at the tetrahedron positions. Ni^{2+} exhibits three spin-allowed transitions at the octahedron positions: $^3A_{2g}$ (^3F) → $^3T_{2g}$ (^3F), $^3A_{2g}$ (^3F) → $^3T_{1g}$ (^3F) and $^3A_{2g}$ (^3F) → $^3T_{1g}$ (^3P) in the ultraviolet–visible region, visible region, and near-infrared region, respectively. The distinct reflection peak in the range of 490–605 nm imparts a yellow-green appearance to $BaZn_{6-x}Ni_xTi_6O_{19}$. When Ni^{2+} occupies the tetrahedron positions, it has three transitions: $^3T_1$ (F) → $^3T_2$ (F), $^3T_1$ (F) → $^3A_2$ (F) and $^3T_1$ (F) → $^3T_1$ (P). Some of these transitions overlap with absorption peaks produced in the octahedron positions of Ni^{2+}. The overlapping of these peaks results in a shift of the reflection peak in the visible light region towards shorter wavelengths, resulting in the darker color of $BaZn_{6-x}Ni_xTi_6O_{19}$. $BaZn_{6-x}Ni_xTi_6O_{19}$ is successfully introduced into PMMA and colorful superhydrophobic coatings, confirming its potential as a novel, green, and environmentally friendly inorganic pigment. This suggests promising applications for $BaZn_{6-x}Ni_xTi_6O_{19}$ in the development of sustainable and eco-friendly coloration solutions.

CRediT authorship contribution statement

Zhiwei Wang: Writing – review & editing, Writing – original draft, Software, Investigation, Formal analysis, Data curation, Conceptualization. **Liangsheng Tian:** Project administration, Methodology, Investigation. **Suwit Suthirakun:** Software, Data curation. **Wongsathorn Kaewraung:** Software, Data curation. **Anjali Verma:** Investigation. **Yaning Yu:** Investigation. **Bin Wang:** Supervision. **Peng Jiang:** Writing – review & editing, Supervision, Resources, Project administration, Funding acquisition. **Hang Zhao:** Software. **Xin Xin:** Software. **M.A. Subramanian:** Writing – review & editing, Supervision, Funding acquisition.

Declaration of competing interest

The authors declare that they have no known competing financial interests or personal relationships that could have appeared to influence the work reported in this paper.

Data availability

Data will be made available on request.

Acknowledgments

Appendix A. Supplementary data

Supplementary data to this article can be found online at https://doi.org/10.1016/j.apsusc.2024.161185.

References

[1] T. Waki, K. Uji, Y. Tabata, H. Nakamura, Single-crystal growth and magnetic properties of Co-substituted Ca-La magnetoplumbite-type ferrite, J. Solid State Chem. 270 (2019) 366–369.
[2] J. Zhang, X. Zhong, Y. Cheng, Y. Wang, Z. Xu, X. Chen, H. Ma, Y. Zhao, X. Cao, Thermal-shock resistance of LnMgAl$_{11}$O$_{19}$ (Ln=La, Nd, Sm, Gd) with magnetoplumbite structure, J. Alloy. Compd. 482 (2009) 376–381.
[3] X. Piao, T. Guo, Z. Zou, J. Liao, H. Wen, G. Guoliang, Site-splitting inhibition and near-infrared luminescence properties of Cr^{3+} activated magnetoplumbite SrAl$_{12}$O$_{19}$ modified by La and Mg, Spectrochim. Acta A Mol. Biomol. Spectrosc. 281 (2022) 121602.
[4] E.A. Medina, J. Li, M.A. Subramanian, Colored oxides with hibonite structure II: Structural and optical properties of CaAl$_{12}$O$_{19}$-type pigments with chromophores based on Fe, Mn, Cr and Cu, Prog. Solid State Chem. 45–46 (2017) 9–29.
[5] G. Costa, M.J. Ribeiro, W. Hajjaji, M.P. Seabra, J.A. Labrincha, M. Dondi, G. Cruciani, Ni-doped hibonite (CaAl$_{12}$O$_{19}$): A new turquoise blue ceramic pigment, J. Eur. Ceram. Soc. 29 (2009) 2671–2678.
[6] J. Li, E.A. Medina, J.K. Stalick, A.W. Sleight, M.A. Subramanian, Colored oxides with hibonite structure: A potential route to non-cobalt blue pigments, Prog. Solid State Chem. 44 (2016) 107–122.
[7] W. Hajjaji, R.C. Pullar, C. Zanelli, M.P. Seabra, M. Dondi, J.A. Labrincha, Compositional and chromatic properties of strontium hexaferrite as pigment for ceramic bodies and alternative synthesis from wiredrawing sludge, Dyes Pigm. 96 (2013) 659–664.
[8] Q. Cheng, X. Chen, L. Liu, P. Jiang, D. Song, M.A. Subramanian, Synthesis and optical properties of Ni/Co/Cr doped BaMg$_6$Ti$_6$O$_{19}$, Ceram. Int. 47 (2021) 34086–34091.
[9] I. Rus, R. Ianoş, R. Lazău, C. Păcurariu, New blue pigments based on Co^{2+} and La^{3+} doped hibonite for NIR-reflective coatings, Mater. Today Chem. 28 (2023).
[10] H. Kojima, Fundamental properties of hexagonal ferrites with magnetoplumbite structure, Handb. Ferromagn. Mater. 3 (1982) 305–391.
[11] T.M. Preethi, R. Ratheesh, Synthesis and dielectric properties of a new class of MX$_6$Ti$_6$O$_{19}$ (M=Ba, Sr and Ca; X=Mg and Zn) ceramics, Mater. Lett. 57 (2003) 2545–2552.
[12] S. Wang, J. Zhai, X. Chou, L. Zhang, X. Yao, Dielectric tunable properties of Ba$_{0.6}$Sr$_{0.4}$TiO$_3$-BaZn$_6$Ti$_6$O$_{19}$ microwave composite ceramics, Mater. Chem. Phys. 115 (2009) 200-203.
[13] G. Pfaff, Inorganic Pigments, Walter de Gruyter GmbH & Co KG2023.
[14] G. Buxbaum, Industrial Inorganic Pigments, John Wiley & Sons, 2008.
[15] A. Larson, R. Von Dreele, Gsas: General structure analysis system report LAUR 86–748, Los Alamos National Laboratory, Los Alamos, NM, 1986.
[16] B.H. Toby, EXPGUI, a graphical user interface for GSAS, J. Appl. Cryst. 34 (2001) 210–213.
[17] G. Kresse, J. Furthmüller, Efficient iterative schemes for ab initio total-energy calculations using a plane-wave basis set, Phys. Rev. B 54 (1996) 11169–11186.
[18] G. Kresse, J. Furthmüller, Efficiency of ab-initio total energy calculations for metals and semiconductors using a plane-wave basis set, Comput. Mater. Sci 6 (1996) 15–50.
[19] P.E. Blöchl, Projector augmented-wave method, Phys. Rev. B 50 (1994) 17953–17979.
[20] J.P. Perdew, K. Burke, M. Ernzerhof, Generalized Gradient Approximation Made Simple, Phys. Rev. Lett. 77 (1996) 3865–3868.
[21] M. Setvin, C. Franchini, X. Hao, M. Schmid, A. Janotti, M. Kaltak, C.G. Van de Walle, G. Kresse, U. Diebold, Direct View at Excess Electrons in TiO$_2$ Rutile and Anatase, Phys. Rev. Lett. 113 (2014) 086402.
[22] Y.-L. Lee, M.J. Gadre, Y. Shao-Horn, D. Morgan, Ab initio GGA+U study of oxygen evolution and oxygen reduction electrocatalysis on the (001) surfaces of lanthanum transition metal perovskites LaBO3 (B = Cr, Mn, Fe, Co and Ni), PCCP 17 (2015) 21643–21663.
[23] Y. Sun, H. Liao, J. Wang, B. Chen, S. Sun, S.J.H. Ong, S. Xi, C. Diao, Y. Du, J.-O. Wang, M.B.H. Breese, S. Li, H. Zhang, Z.J. Xu, Covalency competition dominates the water oxidation structure–activity relationship on spinel oxides, Nat. Catal. 3 (2020) 554–563.
[24] H.J. Monkhorst, J.D. Pack, Special points for Brillouin-zone integrations, Phys. Rev. B 13 (1976) 5188–5192.
[25] A. González-Angeles, G. Mendoza-Suarez, A. Grusková, M. Papánová, J. Slama, Magnetic studies of Zn-Ti-substituted barium hexaferrites prepared by mechanical milling, Mater. Lett. 59 (2005) 26–31.
[26] Z. Wang, C.S. Wang, X.H. Li, H.X. Zeng, (Zn, Ni, Ti) substituted barium ferrite particles with improved temperature coefficient of coercivity, Mater. Sci. Eng. B 90 (2002) 142–145.
[27] M.A. Ahmed, K.E. Rady, M.S. Shams, Enhancement of electric and magnetic properties of Mn–Zn ferrite by Ni–Ti ions substitution, J. Alloy. Compd. 622 (2015) 269–275.
[28] S.-H. Wei, S. Zhang, First-principles study of cation distribution in eighteen closed-shell A^{II}B$_2^{III}$O$_4$ and A^{IV}B$_2^{II}$O$_4$ spinel oxides, Phys. Rev. B 63 (2001).
[29] M.A. Ahmed, E. Ateia, L.M. Salah, A.A. El-Gamal, Structural and electrical studies on La^{3+} substituted Ni–Zn ferrites, Mater. Chem. Phys. 92 (2005) 310–321.
[30] A. Hajalilou, H.M. Kamari, K. Shameli, Dielectric and electrical characteristics of mechanically synthesized Ni-Zn ferrite nanoparticles, J. Alloy. Compd. 708 (2017) 813–826.
[31] M. Kaiser, Electrical conductivity and complex electric modulus of titanium doped nickel-zinc ferrites, Phys. B Condens. Matter 407 (2012) 606–613.
[32] J. Li, H. Zhang, V.G. Harris, Y. Liao, Y. Liu, Ni-Ti equiatomic co-substitution of hexagonal M-type Ba(NiTi)$_x$Fe$_{12-2x}$O$_{19}$ ferrites, J. Alloy. Compd. 649 (2015) 782–787.
[33] R. Ianoş, I. Rus, R. Lazău, C. Păcurariu, Near-infrared reflective Ni, La-doped hibonite pigments for cool blue coatings, Ceram. Int. 48 (2022) 34428–34436.
[34] Y. Wang, Q. Cheng, P. Jiang, L. Liu, K. Cui, Y. Li, Synthesis and properties of novel blue zirconia ceramic based on Co/Ni-doped BaAl$_{12}$O$_{19}$ blue chromophore, J. Eur. Ceram. Soc. 42 (2022) 543–551.
[35] Q. Cheng, X. Chen, P. Jiang, Q. Wang, Z. Wang, M.A. Subramanian, Synthesis and properties of blue zirconia ceramic based on Ni/Co doped Ba$_{0.956}$Mg$_{0.912}$Al$_{10.088}$O$_{17}$ blue pigments, J. Eur. Ceram. Soc. 42 (2022) 4311–4319.
[36] N. Jayababu, M. Poloju, J. Shruthi, M.V.R. Reddy, Semi shield driven p-n heterostructures and their role in enhancing the room temperature ethanol gas sensing performance of NiO/SnO$_2$ nanocomposites, Ceram. Int. 45 (2019) 15134–15142.
[37] F. Jiang, J. Yu, J. Feng, J. Chen, T. Wang, X. Zhang, Q. Zhang, R. Zhang, Q. Wu, Q. Hu, Y. Yu, J. Liu, Synthesis and coloring properties of novel stablized green Ni$_{0.15}$Mg Al$_{2(0.85-x)}$Ti$_{1.15+x}$O$_5$ pigments, J. Eur. Ceram. Soc. 43 (2023) 4179–4188.
[38] J. Chen, G. Feng, F. Jiang, L. Yin, Q. Zhao, S. Lan, X. Zhang, J. Liu, Q. Hu, W. Jiang, Synthesis and coloring properties of novel Ni-doped tialite pigments, Ceram. Int. 47 (2021) 33242–33251.
[39] M. Bukhtiyarova, A. Ivanova, E. Slavinskaya, P. Kuznetsov, L. Plyasova, O. Stonkus, V. Rogov, V. Kaichev, A. Noskov, Steam reforming of methane over Ni-substituted Sr hexaaluminates, Catalysis for Sustainable Energy 1 (2012).
[40] B. Huang, Y. Xiao, H. Zhou, J. Chen, X. Sun, Synthesis and Characterization of Yellow Pigments of Bi$_{1.7}$RE$_{0.3}$W$_{0.7}$Mo$_{0.3}$O$_6$ (RE = Y, Yb, Gd, Lu) with High NIR Reflectance, ACS Sustain. Chem. Eng. 6 (2018) 10735–10741.
[41] M. Llusar, E. García, M.T. García, C. Gargori, J.A. Badenes, G. Monrós, Stability and coloring properties of Ni-qandilite green spinels (Ni, Mg)2TiO4: The "half color wheel" of Ni-doped magnesium titanates, Dyes Pigm. 122 (2015) 368–381.
[42] S.K. Biswas, D. Dhak, A. Pathak, P. Pramanik, Chemical synthesis of environment-friendly nanosized yellow titanate pigments, Mater. Res. Bull. 43 (2008) 665–675.
[43] M. Llusar, E. García, M.T. García, C. Gargori, J.A. Badenes, G. Monrós, Synthesis, stability and coloring properties of yellow-orange pigments based on Ni-doped karrooite (Ni, Mg)Ti$_2$O$_5$, J. Eur. Ceram. Soc. 35 (2015) 357–376.
[44] M. Llusar, E. García, M.T. García, V. Esteve, C. Gargori, G. Monrós, Synthesis and coloring performance of Ni-geikielite (Ni, Mg)Ti$_O$3 yellow pigments: effect of

temperature, Ni-doping and synthesis method, J. Eur. Ceram. Soc. 35 (2015) 3721–3734.

[45] Y. Tanabe, S. Sugano, On the Absorption Spectra of Complex Ions I, J. Phys. Soc. Japan 9 (1954) 753–766.

[46] E. König, The nephelauxetic effect calculation and accuracy of the interelectronic repulsion parameters I. Cubic high-spin d^2, d^3, d^7, and d^8 systems, Structutal and Bonding, Springer, 1971, pp. 175–212.

[47] F. Jiang, J. Yu, G. Feng, J. Chen, T. Wang, X. Zhang, Q. Zhang, R. Zhang, Q. Wu, Q. Hu, Y. Yu, J. Liu, Synthesis and coloring properties of novel stablized green $Ni_{0.15}Mg_xAl_{2(0.85-x)}Ti_{1.15+x}O_5$ pigments, J. Eur. Ceram. Soc. 43 (2023) 4179–4188.

[48] G. George, L. Sandhya Kumari, V.S. Vishnu, S. Ananthakumar, M.L.P. Reddy, Synthesis and characterization of environmentally benign calcium-doped $Pr_2Mo_2O_9$ pigments: Applications in coloring of plastics, J. Solid State Chem. 181 (2008) 487–492.

[49] Y. Jia, B. Chen, M. Zhang, X. Li, J. Yang, A novel colorful sepiolite-based superhydrophobic coating with excellent mechanical and chemical stability and self-cleaning property, Mater. Lett. 254 (2019) 340–343.

[50] H. Liu, F. Wang, S. Lei, J. Ou, W. Li, Large-area fabrication of colorful superhydrophobic coatings with high solar reflectivity, Constr. Build. Mater. 304 (2021).